Catalysis Today 241 (2015) 25–32

Contents lists available at ScienceDirect

Catalysis Today

journal homepage: www.elsevier.com/locate/cattod

Influence of the sol–gel preparation method on the photocatalytic NO oxidation performance of TiO_2/Al_2O_3 binary oxides

Meryem Polat[a], Asli M. Soylu[a], Deniz A. Erdogan[a], Huseyin Erguven[a], Evgeny I. Vovk[a,b], Emrah Ozensoy[a,*]

[a] Department of Chemistry, Bilkent University, 06800 Ankara, Turkey
[b] Boreskov Institute of Catalysis, 630090 Novosibirsk, Russian Federation

ARTICLE INFO

Article history:
Received 10 January 2014
Received in revised form 20 March 2014
Accepted 2 April 2014
Available online 13 May 2014

Keywords:
TiO_2
Al_2O_3
Air purification
Photocatalysis
NO
NO_2

ABSTRACT

In the current work, TiO_2/Al_2O_3 binary oxide photocatalysts were synthesized via two different sol–gel protocols (P1 and P2), where various TiO_2 to Al_2O_3 mole ratios (0.5 and 1.0) and calcination temperatures (150–1000 °C) were utilized in the synthesis. Structural characterization of the synthesized binary oxide photocatalysts was also performed via BET surface area analysis, X-ray diffraction (XRD) and Raman spectroscopy. The photocatalytic NO(g) oxidation performances of these binary oxides were measured under UVA irradiation in a comparative fashion to that of a Degussa P25 industrial benchmark. TiO_2/Al_2O_3 binary oxide photocatalysts demonstrate a novel approach which is essentially a fusion of NSR (NO_x storage reduction) and PCO (photocatalytic oxidation) technologies. In this approach, rather than attempting to perform complete NO_x reduction, NO(g) is oxidized on a photocatalyst surface and stored in the solid state. Current results suggest that alumina domains can be utilized as active NO_x capturing sites that can significantly eliminate the release of toxic NO_2(g) into the atmosphere. Using either (P1) or (P2) protocols, structurally different binary oxide systems can be synthesized enabling much superior photocatalytic total NO_x removal (i.e. up to 176% higher) than Degussa P25. Furthermore, such binary oxides can also simultaneously decrease the toxic NO_2(g) emission to the atmosphere by 75% with respect to that of Degussa P25. There is a complex interplay between calcination temperature, crystal structure, composition and specific surface area, which dictate the ultimate photocatalytic activity in a coordinative manner. Two structurally different photocatalysts prepared via different preparation protocols reveal comparably high photocatalytic activities implying that the active sites responsible for the photocatalytic NO(g) oxidation and storage have a non-trivial nature.

1. Introduction

Air pollution in the urban settings leads to significantly detrimental implications on human health. Some of the main air borne contaminants in the atmosphere are nitrogen oxides (NO_x), sulfur oxides (SO_x), volatile organic compounds (VOCs) and particulate matter (PM) [1]. NO_x-based contaminants are emitted to the atmosphere through various anthropological, industrial or natural combustion processes [1–3]. Under atmospheric conditions, NO(g) can be homogeneously oxidized to NO_2(g) via thermal (non-catalytic) chemical pathways. NO_2(g) is considered to be even more toxic than NO(g), as it can cause asthma and many other respiratory illnesses [4]. In the last few decades, various technologies have been developed in order to reduce airborne toxic NO_x species which include selective non-catalytic reduction (SNCR), selective catalytic reduction (SCR), NO_x Storage and Reduction (NSR) (also called Lean NO_x Traps, LNT) and Three Way Catalysis (TWC) technologies [4–13]. However, almost without exception, these technologies are effective only at elevated temperatures (i.e. $T \geq 250$ °C).

Heterogeneous photocatalytic oxidation (PCO) is an alternative approach that can be utilized under ambient conditions (i.e. room temperature and atmospheric pressures) for air and water purification [14–18]. A large variety of photocatalytic materials that can provide air purification under UV or visible light excitation have been reported in the literature [15,19–28]. TiO_2-based materials are among the most effective photocatalysts operating under ambient conditions for air purification applications [15,22,25,26,29]. However, TiO_2 is also known to have some drawbacks, such as poor mechanical properties and low specific surface area (SSA), which limit its catalytic performance [30–32].

* Corresponding author. Tel.: +90 3122902121.
E-mail address: ozensoy@fen.bilkent.edu.tr (E. Ozensoy).

http://dx.doi.org/10.1016/j.cattod.2014.04.001
0920-5861/

In a recent study, we have reported a TiO_2/Al_2O_3 binary oxide system demonstrating a promising gas-phase photocatalytic $DeNO_x$ performance, which was found to be superior to a commercial TiO_2 (Degussa P25) benchmark photocatalyst [33,34]. This material was designed to demonstrate a novel approach which is essentially a fusion of NSR and PCO technologies. In this approach, rather than attempting to perform complete NO_x reduction, NO_x is oxidized on a photocatalyst surface and stored in the solid state in the form of nitrates and nitrites on a storage component. Unlike the photocatalytic metal-oxide surface, which is not water-soluble, stored nitrates and nitrites (or their protonated surface derivatives) can be readily washed off the photocatalyst surface (e.g. via rain or wet scrubbing), restoring the photocatalytic activity of the surface and regenerating the photocatalyst.

Chemical and structural properties of the binary oxide systems strongly influence the NO_x oxidation and storage capacity [16,18]. Along these lines, in the current work, we focus on TiO_2/Al_2O_3 binary oxide photocatalysts which are synthesized using two different sol–gel routes (i.e. P1 and P2) and thermally treated at various temperatures. The first family of TiO_2/Al_2O_3 binary oxide materials prepared via P1 manifests itself as inhomogeneously dispersed TiO_2 crystallites deposited on alumina, while the second one prepared via P2 is a mostly amorphous sponge-like $Al_xTi_yO_z$ mixed oxide with a more homogenous morphology [35]. Thus, in the current contribution, the influence of the photocatalyst binary oxide structure on the photocatalytic performance and NO_x storage capability are investigated. Photocatalytic performances of these two different families of TiO_2/Al_2O_3 binary oxides are also compared to a commercial benchmark photocatalyst (i.e. Degussa P25) in order to show that photocatalytic $NO_x(g)$ abatement can be significantly improved by utilizing TiO_2/Al_2O_3 binary oxide systems.

2. Experimental

2.1. Preparation and structural characterization of TiO_2/Al_2O_3 binary oxides

TiO_2/Al_2O_3 binary oxide materials were prepared by two different sol–gel synthesis protocols denoted as P1 and P2 which were described in detail in our earlier reports [11,12,33,35]. Briefly, in the first synthetic protocol (P1), γ-Al_2O_3 (PURALOXS Ba200, 200 m^2/g, SASOL GmbH, Germany) and $TiCl_4$ (Fluka, titanium (IV) chloride solution) were used as starting materials. In order to form a gel, 25 vol% NH_3 was added to the aqueous γ-Al_2O_3 and $TiCl_4$ mixture under constant stirring. In the second protocol (P2), titanium (IV) isopropoxide (TIP, 97%, Sigma–Aldrich) and aluminum tri-sec-butoxide (ASB, 97%, Sigma–Aldrich) were used as precursors. Synthesized P1 and P2 materials were subsequently calcined in air for 2 h at temperatures ranging between 150 and 1000 °C. In the synthesized materials, TiO_2 to Al_2O_3 mole ratios were adjusted to be either 0.5 or 1.0. These ratios were chosen based on our previous studies, which indicated that for (P2) Ti/Al materials, TiO_2 to Al_2O_3 mole ratios of 0.5 and 1.0 yielded some of the best performing photocatalysts [33]. Currently synthesized samples are labeled as "(P#) n Ti/Al-T", where P# denotes the utilized synthesis protocol (i.e. P1 or P2), n stands for the TiO_2 to Al_2O_3 mole ratio (i.e. 0.5 or 1.0) and T corresponds to the calcination temperature in Celsius scale. A commercially obtained TiO_2 photocatalyst (Degussa P25, 99.5%, Sigma–Aldrich) comprised of approximately 80–85% anatase and 15–20% rutile by mass; was also used as a benchmark sample in order to compare photocatalytic activities of different samples under identical photocatalytic conditions [36].

BET specific surface area measurements were performed using a Micromeritics Tristar 3000 surface area and pore size analyzer via low-temperature isothermal adsorption–desorption of N_2. Before the surface area measurements, materials were outgassed in vacuum at 350 °C for 4 h. The powder X-ray diffraction (XRD) patterns were recorded using a Rigaku powder diffractometer, equipped with a Miniflex goniometer and an X-ray source with CuK_α radiation, λ = 1.5418 Å, 30 kV, and 15 mA. The XRD patterns were recorded in the 2θ range of 10–60° with a scan rate of 0.02° s^{-1}. Diffraction patterns were assigned using Joint Committee on Powder Diffraction Standards (JCPDS) cards supplied by the International Centre for Diffraction Database (ICDD). Raman spectra were recorded using a HORIBA Jobin Yvon LabRam HR 800 spectrometer, equipped with a confocal Raman BX41 microscope and a CCD detector. The Raman spectrometer was also equipped with a Nd:YAG laser (λ = 532.1 nm); the laser power was adjusted to 20 mW for data acquisition.

2.2. Gas phase photocatalytic activity measurements

A custom-design photocatalytic flow reactor system was used in the photocatalytic activity measurements [33,37]. The flow reactor system consisted of a gas manifold system, mass flow controllers (MKS 1479A), a capacitance pressure gauge (MKS Baratron 622B), a custom-made photocatalytic reactor and a chemiluminescence NO_x analyzer (Horiba APNA 370). The gas manifold system was connected to gas cylinders containing $N_2(g)$ (99.998%, Linde GmbH), $O_2(g)$ (99.998%, Linde GmbH), and 100 ppm NO diluted in $N_2(g)$ (Linde GmbH). Mass flow controllers (MFC) calibrated for N_2 and O_2 gases were used to control the volumetric flow rates of the gases. Flow rate of the gases were adjusted to 0.750 standard liters per minute (SLM) for $N_2(g)$, 0.250 SLM for $O_2(g)$ and 0.010 SLM for the mixture of 100 ppm NO(g) diluted in $N_2(g)$. The mixed gases were bubbled through a thermostatic humidifier filled with deionized water which was kept at 25 °C. The relative humidity of the total gas mixture was 70% which was measured at the sample position in the flow reactor with a Hanna HI 9565 humidity analyzer. For a typical photocatalytic performance measurement, 950 mg of a powder sample was placed on a 2 mm × 40 mm × 40 mm polymethyl methacrylate (PMMA) planar sample holder and the gas mixture was allowed to sweep over the photocatalyst powder which was packed into the sample holder. Before the photocatalytic performance measurements, the embedded TiO_2/Al_2O_3 samples were irradiated with UVA light (F8W/T5/BL368, Sylvania or F8W/T5/BL350, Sylvania) under atmospheric conditions for 18 h in order to remove the surface contaminations and to activate the photocatalysts. After this initial ex situ pretreatment step, activated photocatalyst powders were placed in the flow reactor which was equipped with an 8 W UVA lamp. During the performance analysis experiments, (P1) Ti/Al samples were irradiated with a 368 nm wavelength light source (F8W/T5/BL368, Sylvania, Germany) and (P2) Ti/Al samples were irradiated with a 350 nm wavelength light source (F8W/T5/BL350, Sylvania, Germany). For both cases, photocatalytic performances of the Ti/Al photocatalysts were normalized using the photocatalytic performance values of the Degussa P25 benchmark samples, which were measured under the identical photocatalytic conditions using the corresponding UVA light source utilized in the Ti/Al sample measurements.

For the determination of the relative photocatalytic performances, per cent photonic efficiencies (ζ%) were utilized which are described in Eqs. (1) and (2).

$$\zeta\% = \left(\frac{n_{NO_x}}{n_{photon}}\right) \times 100 \quad (1)$$

where, n_{NO_x} represents either the decrease in the total number of moles of all gaseous NO_x species or the number of moles of $NO_2(g)$ generated in a 60 min photocatalytic activity test. Furthermore, n_{photon} corresponds to the total number of moles of incident UVA

photons impinging on the photocatalyst surface in 60 min, which is calculated via Eq. (2) as:

$$n_{\text{photon}} = \frac{I\lambda St}{Nhc} \quad (2)$$

where I stands for the power density of the UVA lamp experimentally measured at the sample position in the photocatalytic reactor (typically, 7.5 W m^{-2}), λ is the representative emission wavelength of the UVA lamp (i.e. 350 nm or 368 nm), S is the surface area of the planar PMMA sample holder in the reactor that is exposed to the UVA irradiation (i.e. 40 mm × 40 mm = 1600 mm^2); t is the duration of the performance test (i.e. 3600 s), N is the Avogadro's number, h is Planck's constant and c is the speed of light.

In the current work, experimentally measured per cent photonic efficiencies of (P1) Ti/Al samples were normalized by using the per cent photonic efficiency values of the Degussa P25 benchmark photocatalyst (Supporting Information Fig. S1) whose photocatalytic performance was measured under identical flow and illumination conditions with the (P1) Ti/Al samples. Thus, normalized photocatalytic performances of the (P1) Ti/Al samples were reported by dividing the per cent photonic efficiency of the (P1) Ti/Al sample to the per cent photonic efficiency of Degussa P25 benchmark photocatalyst and by multiplying this ratio by 100, as shown in Eq. (3):

$$\%\,\text{relative photonic efficiency of (P1) Ti/Al with respect to P25} = \left(\frac{\zeta\%_{(\text{P1})\text{Ti/Al}}}{\zeta\%_{\text{P25}}}\right) \times 100 \quad (3)$$

The same approach was also followed for the (P2) Ti/Al family, where the normalized photocatalytic activity values of the (P2) Ti/Al samples were reported using the per cent photonic efficiency values of the Degussa P25 benchmark sample (Supporting Information Fig. S1) which was analyzed under identical flow and illumination conditions with the (P2) Ti/Al family.

Note that all of the reported photocatalytic performance measurements in this work correspond to 950 mg of photocatalyst. In other words, these values are *intentionally* neither normalized using the photocatalyst specific surface area nor using the photocatalyst mass. Drawbacks associated with the normalization of the photocatalytic reaction rates using photocatalyst mass was discussed recently in detail by Wachs et al. [38]. We believe that normalization of the photocatalytic activity values in the current study via SSA could also be quite misleading; as the overall SSA of the currently employed complex mixed oxide heterogeneous catalysts may *not* be simply related to the specific surface areas of the active phase(s). Furthermore, to the best of our knowledge, the exact chemical/electronic/morphological nature of the active site(s) responsible for the photocatalytic NO_x oxidation and storage on TiO_2/Al_2O_3 binary oxides are also not clear [39–46]. This complication also prevents an unambiguous experimental determination of the surface coverage of the active sites, precluding the unequivocal calculation of a turn over frequency (TOF) value. Furthermore, another additional complication regarding the comparison of absolute photocatalytic activities of different powder photocatalysts in a gas/solid photochemical reaction is associated with the macroscopic packing of the micron/millimeter-sized grains that are forming the powder samples. Due to the macroscopic grain size and grain density distribution differences, light penetration/scattering toward the grains which are physically located farther from the PMMA sample holder surface level varies in a complex manner. This suggests that macroscopic grain size and grain packing density of different photocatalyst powders are important parameters that play an active role in the magnitude of the absolute photonic efficiency values. Considering all of these complications, we believe that reporting photocatalytic activity values as described in Eqs. (1)–(3) provides a relatively unambiguous comparison of the (P1) Ti/Al, (P2) Ti/Al and Degussa P25 samples. In the light of this approach, by considering the relative performance of Ti/Al samples with respect to P25; one can also readily compare Ti/Al binary oxide samples with many other existing photocatalytic systems reported in the literature.

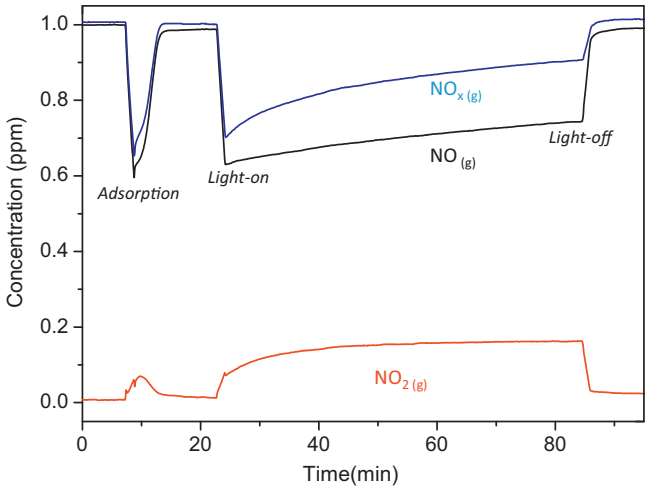

Fig. 1. Concentration versus time plot for a representative photocatalytic performance test. Blue, black and red curves correspond to the concentrations of total NO_x(g), NO(g) and NO_2(g), respectively (see text for details). (For interpretation of the references to color in figure legend, the reader is referred to the web version of the article.)

In the photocatalytic performance analysis tests, concentrations versus time plots acquired by the chemiluminescence NO_x analyzer were exploited. Fig. 1 illustrates a typical concentration versus time plot recorded during a photocatalytic performance test. In this plot, (blue-colored) total NO_x concentration (i.e. sum of the concentrations of all of the NO_x species existing in the reactor) as well as NO(g) (black curve) and NO_2(g) (red curve) concentrations in the photocatalytic reactor are presented as a function of time. In the first ~20 min of the analysis, a gas mixture containing N_2(g), O_2(g), H_2O(g) and 1 ppm NO(g) is supplied to the photocatalyst surface under dark conditions, where the UVA lamp is off and any background light exposure of the photocatalyst surface is prevented. In this period (i.e. at $t \sim 7$ min), gas feed is switched from the by-pass line to the reactor which is accompanied by a transient decrease in the total NO_x(g) and NO(g) concentrations. This can be attributed to the dilution of the gas in the reactor and the adsorption of NO_x species on the gas lines, reactor walls as well as adsorption on the photocatalyst surface. Since under these conditions no UV or VIS radiation is allowed to impinge on the photocatalyst surface, no photocatalytic activity is observed during this initial stage, evident by the presence of a minor amount of NO_2(g) production which is mostly due to thermal catalytic oxidation processes occurring on the catalyst surface. After this initial dark period, reactor walls and the photocatalyst surface are saturated with NO_x, which is apparent by the return of the NO_x(g) and NO(g) traces to the original inlet concentration value of c.a. 1 ppm, signifying the end of the thermal catalytic activity.

After this initial transient period that is at $t \sim 25$ min, UVA irradiation is turned on and the photocatalytic reaction is started. Due to the UVA illumination, a significant and a permanent decrease in the NO(g) and total NO_x(g) concentrations concomitant to a visible permanent rise in the NO_2(g) level are observed. This indicates the conversion of NO(g) into NO_2(g) via PCO process. Furthermore, produced NO_2(g) can adsorb on the photocatalyst surface in the form of chemisorbed NO_2, nitrites and nitrates [11,12,35] and stored in the solid state, resulting in a further fall in the NO(g) and total NO_x

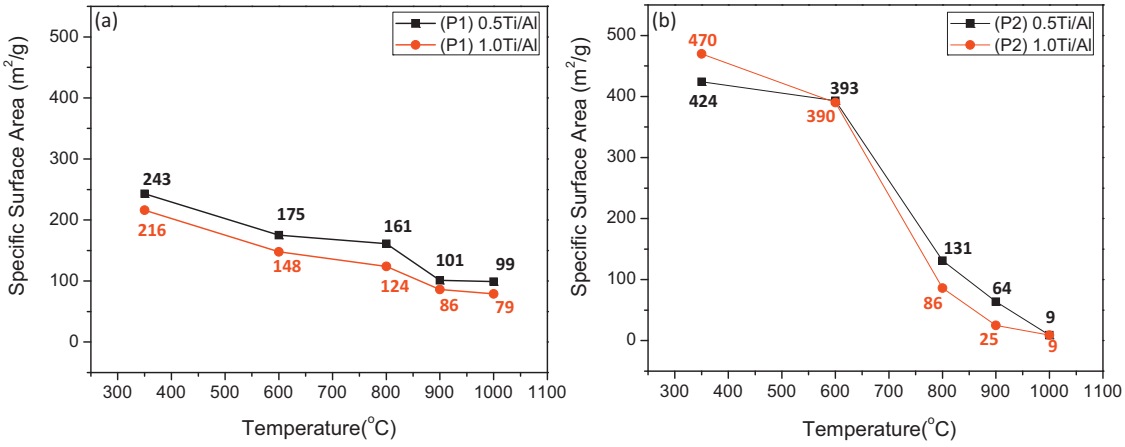

Fig. 2. Specific surface area values for the synthesized (a) (P1) Ti/Al and (b) (P2) Ti/Al binary oxide samples after calcination at various temperatures.

signals. It should be noted that, decrease in the NO(g) concentration might also have some contribution from the direct photocatalytic decomposition and photo-reduction of NO(g) forming N_2(g) and/or N_2O(g) [47]. However, since the direct photocatalytic reduction is a relatively inefficient pathway, this reaction channel may be expected to be a minor photochemical route. Consequently, the total NO_x concentration (blue) curve (which is mostly comprised of the sum of NO(g) and NO_2(g) signals) in Fig. 1 remains mostly below 1 ppm during the UVA-activated regime, illustrating the continuous photocatalytic activity and photochemical NO_x storage in the solid state.

3. Results and discussion

Thermal evolution and the structural changes of the (P1) Ti/Al and (P2) Ti/Al samples were studied as a function of the calcination temperatures. The specific surface areas (SSA) of the synthesized Ti/Al binary oxides calcined at different temperatures are presented in Fig. 2. Before calcination (P2) Ti/Al samples have significantly (almost two times) higher SSA values than the corresponding (P1) Ti/Al samples. This difference can be associated with dissimilar morphologies of P1 and P2 samples. TEM-EDX analysis of Ti/Al samples synthesized via P1 and P2 suggests that (P1) Ti/Al material consists of TiO_2 crystallites dispersed rather inhomogeneously on γ-Al_2O_3, while (P2) Ti/Al material presents a more homogenous and an amorphous $Al_xTi_yO_z$ mixed oxide system with a higher porosity [35]. The SSA values of both (P1) and (P2) Ti/Al binary oxides drastically decrease in a monotonic fashion with increasing calcination temperature. As will be shown below via XRD data (Fig. 3), this monotonic decrease in SSA values is associated with the ordering and crystallization of the mixed oxide system and formation of new phases. Another important behavior observed in Fig. 2 is that for lower calcination temperatures the Ti/Al mixed oxides prepared via P2 reveal much higher SSA values compared to that of P1; for higher calcination temperatures this trend is reversed and P2 samples continue to lose SSA in a radical manner while SSA loss for P1 samples remain at a moderate level. This is due to the fact that in the P1 materials, titania is dispersed onto the γ-Al_2O_3 support material where alumina and titania domains exist as separate phases. In this system, γ-Al_2O_3 serves as a strong

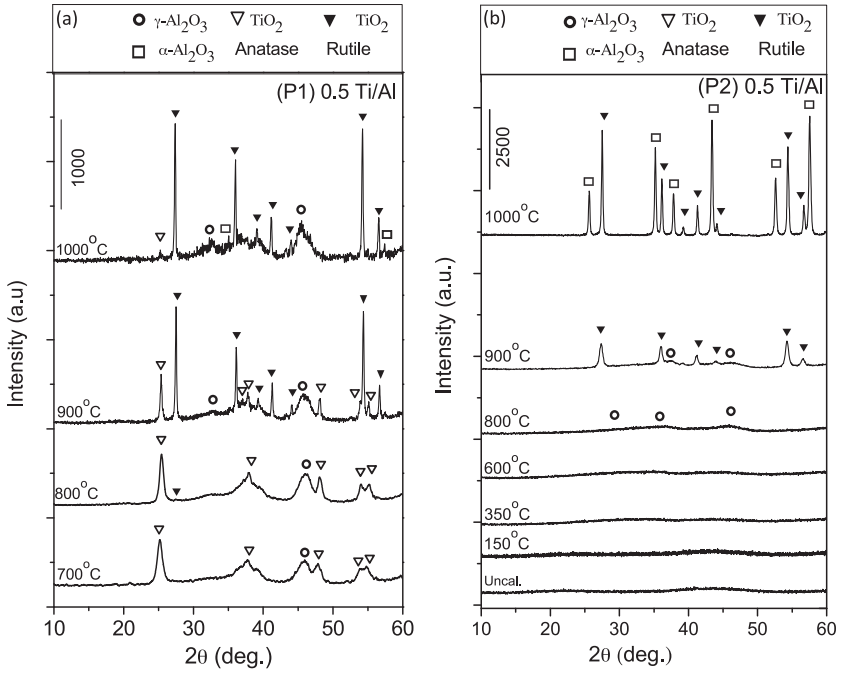

Fig. 3. XRD patterns corresponding to the (a) (P1) 0.5 Ti/Al and (b) (P2) 0.5 Ti/Al binary oxide samples after calcination at various temperatures.

backbone enabling a relatively high intrinsic sintering resistance, where γ-Al_2O_3 → α-Al_2O_3 (corundum) and TiO_2 (anatase) → TiO_2 (rutile) phase transitions are hindered (Fig. 3). In contrast, P2 system is comprised of a $Al_xTi_yO_z$ mixed oxide which can readily form low-surface area phases such as corundum and rutile at elevated temperatures (Fig. 3).

Structural alterations of the (P1) and (P2) Ti/Al photocatalysts were also investigated as a function calcination temperature via XRD method (Fig. 3). Fig. 3 shows the representative XRD patterns of these binary oxide samples with a titania to alumina mole ratio of 0.5. It can be seen in Fig. 3a that the (P1) 0.5 Ti/Al-700 sample yields broad diffraction peaks corresponding to anatase phase (JCPDS 21-1272) and even broader diffraction signals associated with γ-Al_2O_3 (JCPDS 29-0063) indicating small crystallite sizes. Further calcination at 800 °C, does not result in a significant change in the XRD pattern of the (P1) Ti/Al system. However, calcination at 900 °C leads to the sharpening of the anatase diffraction signals suggesting crystallographic ordering of this particular phase. Furthermore, at this calcination temperature, sharp and intense rutile diffraction signals (JCPDS 04-0551) also become apparent; clearly demonstrating the beginning of an anatase → rutile phase transformation. Calcination of the (P1) 0.5 Ti/Al sample at 1000 °C leads to significant suppression of anatase diffraction signals, along with the formation of weak but discernible α-Al_2O_3 (corundum) phase (JCPDS 10-0173). It is worth mentioning that the corresponding XRD patterns of the (P1) 1.0 Ti/Al sample reveal identical crystallographic trends to that of the (P1) 0.5 Ti/Al sample and hence are not be shown here (Supporting Information Fig. S2).

Fig. 3b shows XRD patterns of the (P2) 0.5 Ti/Al photocatalysts calcined at various temperatures. It is apparent in Fig. 3b that upon calcination at temperatures below 900 °C, (P2) 0.5 Ti/Al system reveals a mostly amorphous structure and relatively disordered phases with small particle sizes. Calcination of the (P2) 0.5 Ti/Al sample at 900 °C leads to the formation of the rutile phase. It should be noted that in the (P2) 0.5 Ti/Al system, amorphous $Al_xTi_yO_z$ mixed oxide transforms readily into the rutile phase without revealing a substantial amount of anatase. Increasing the calcination temperature to 1000 °C, results in the sharpening and strengthening of the rutile signals and formation of intense α-Al_2O_3 signals. XRD patterns of the (P2) 1.0 Ti/Al sample (data not shown) reveal analogous trends to the ones given in Fig. 3b where the only noticeable difference is the shift in the onset of the crystallization/ordering temperature to 800 °C; as a result of the increasing titania loading in the binary oxide mixture.

Comparison of the thermally induced structural changes of (P1) Ti/Al and (P2) Ti/Al samples reveals that for the (P1) Ti/Al sample, anatase phase exists in a larger thermal window in contrast to the (P2) Ti/Al system. In addition, although corundum formation is observed in a rather limited fashion on the (P1) Ti/Al system within the investigated thermal window, presence of corundum is much more significant for the (P2) Ti/Al system. Furthermore, XRD data given in Fig. 3 are in very good agreement with the BET results presented in Fig. 2. It is apparent that the drastic fall in the SSA values of the (P2) Ti/Al system at elevated calcination temperatures can be linked to the formation of highly crystalline and low-surface area phases such as rutile and corundum, while such phases are not expressed in a strong fashion for the (P1) Ti/Al system.

Fig. 4 presents Raman spectra of the synthesized (P1) and (P2) 0.5 Ti/Al samples after calcination at various temperatures. Raman spectrum of the (P1) 0.5 Ti/Al sample calcined at 700 °C given in Fig. 4a shows weak Raman features at 144, 400, 519 and 639 cm^{-1} which can be readily assigned to the anatase phase [11]. Increasing the calcination temperature to 800 °C leads to sharper and more intense anatase Raman signals suggesting ordering and further crystallization of this particular phase. Calcination of the (P1) 0.5 Ti/Al sample at 900 °C results in a decrease in the relative intensities of anatase signals while new Raman features associated with rutile phase start to appear at 236, 447 and 612 cm^{-1} [11]. Further calcination at 1000 °C leads to almost complete suppression of the anatase features while rutile signals significantly intensify (Fig. 4a) in very good agreement with the corresponding XRD data presented in Fig. 3a.

For the (P2) 0.5 Ti/Al samples, no Raman bands were detected for calcination temperatures less than or equal to 600 °C (Fig. 4b).

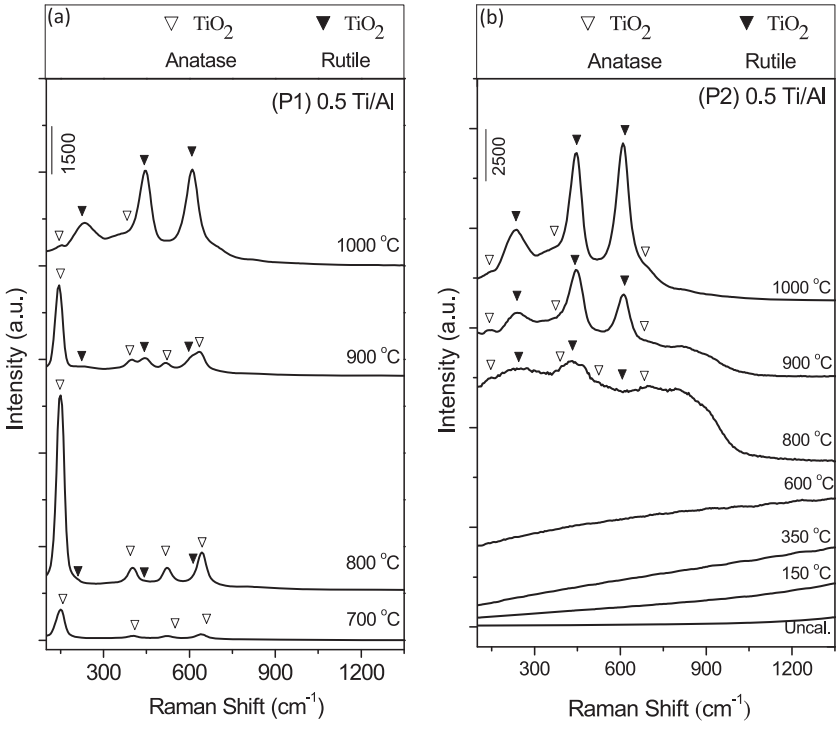

Fig. 4. Raman spectra corresponding to the (a) (P1) 0.5 Ti/Al and (b) (P2) 0.5 Ti/Al binary oxide samples after calcination at various temperatures.

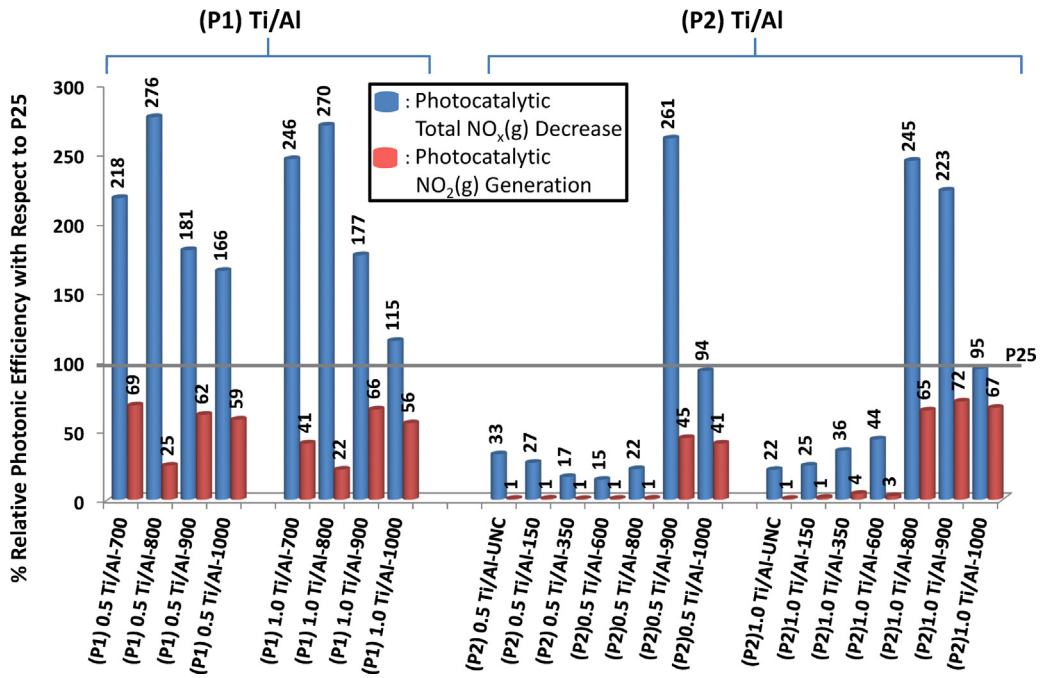

Fig. 5. Relative photocatalytic performances of the synthesized Ti/Al binary oxide samples normalized with respect to the photocatalytic activity of Degussa P25 industrial benchmark (see text for details).

On the other hand, calcination at 800 °C yields a complicated and convoluted set of Raman bands which contain both anatase and rutile features. It should be noted that such features are elusive to detect in the corresponding XRD data presented in Fig. 3b suggesting the presence of relatively small and disordered anatase and rutile crystallites at this temperature. At higher calcination temperatures such as 900 °C and 1000 °C, (P2) 0.5 Ti/Al sample is dominated by the rutile phase along with the gradual disappearance of the anatase phase; in accordance with the corresponding XRD data presented in Fig. 3b.

Photocatalytic NO oxidation and storage performances of all of the synthesized binary oxide samples as well as the Degussa P25 benchmark photocatalyst were also measured in the custom-design photocatalytic flow reactor. Per cent photonic efficiencies for "Photocatalytic total NO_x(g) decrease" and "Photocatalytic NO_2(g) generation" were calculated by integrating the time versus concentration plots similar to the one given in Fig. 1 and using Eqs. (1) and (2). Next, per cent photonic efficiency values of the Ti/Al samples were normalized using the corresponding values of the P25 Degussa benchmark catalyst as described in Eq. (3). These values are denoted as "% Relative photonic efficiency with respect to P25". Fig. 5 presents these normalized per cent photonic efficiency values for "Photocatalytic Total NO_x Decrease" (blue bars) and for "Photocatalytic NO_2(g) Generation" (red bars). In this normalized vertical axis, 100% corresponds to a photocatalytic activity that is identical to that of Degussa P25 benchmark photocatalyst (illustrated by the horizontal flat line in the histogram).

Note that for an ultimate photocatalyst with a supreme $DeNO_x$ performance, blue bars should be maximized (to obtain maximum photocatalytic NO_x(g) storage/conversion); while red bars should be simultaneously minimized (to release minimum amount of toxic NO_2(g) into the atmosphere). Degussa P25 benchmark photocatalyst has a high photocatalytic NO(g) oxidation ability leading to the generation of large quantities of unwanted NO_2(g) along with a very limited NO_x storage capability (Supporting Information Fig. S1). Keeping in mind that NO_2(g) is a much more toxic chemical than NO(g), high photocatalytic NO oxidation activity of the Degussa P25 industrial benchmark photocatalyst without a significant NO_x storage capability renders this material a non-ideal NO_x removal photocatalyst.

Analysis of the performance results presented in Fig. 5 reveals interesting observations. For all of the synthesized Ti/Al binary oxide systems, NO_2(g) slip to the atmosphere (i.e. red bars in Fig. 5) is always less than that of the Degussa P25 benchmark photocatalyst. This observation may have two different origins. Firstly, for a large number of the analyzed Ti/Al samples, overall photocatalytic NO oxidation and further NO_2 storage in the form of nitrates/nitrites are greater than that of P25 (this is evident by the blue bars above 100% mark, concomitant to the red bars below the 100% mark). For these systems, although a large amount of NO_2 is generated via photocatalytic NO oxidation, these oxidized species cannot find the opportunity to slip into the atmosphere due to the high NO_x storage capacity of the binary oxide system provided by the alumina domains which are able to rapidly capture the oxidized NO_x species in the solid state. This is also consistent with the fact that NO_x adsorption energy on alumina is typically higher than that of titania [12]. The second origin of the relatively low NO_2 slip of a small group of Ti/Al samples (such as (P2) 0.5 Ti/Al and (P2) 1.0 Ti/Al samples calcined at $T < 800$ °C) are associated with the fact that these photocatalysts have an extremely poor photocatalytic NO oxidation capability. Since these photocatalysts cannot generate NO_2(g) via photocatalytic oxidation (verified by small blue bars in Fig. 5), NO_2 slip is accordingly also very limited. Thus in general, performance data in Fig. 5 indicate that for highly active photocatalysts which can efficiently convert NO(g) into NO_2(g), alumina domains can be utilized as active NO_x capturing sites that can significantly eliminate the release of toxic NO_2(g) into the atmosphere by adsorption and solid state storage. As will be discussed in more detail below, alumina addition also typically improves the SSA of the binary oxide systems (Fig. 2) and enables them to have generally higher SSA values than that of Degussa P25 (i.e. 55 m^2/g). On the other hand, it is also worth mentioning that in the absence of a photocatalytic oxidation component such as TiO_2, pure γ-Al_2O_3 has an extremely limited photocatalytic

NO(g) storage/adsorption and NO_2(g) generation capability (data not shown). This observation clearly demonstrates the need for the co-existence of photocatalytic NO(g) → NO_2(g) oxidation functionalities together with NO_2(g) adsorption/storage functionalities in an ultimate photocatalyst.

In order to investigate the effect of calcination temperature on the photocatalytic performance of the Ti/Al systems, one can focus on the corresponding data for the (P2) 0.5 Ti/Al photocatalyst family given in Fig. 5. Assessment of this set of data clearly reveals that for calcination temperatures less than 900 °C, (P2) 0.5 Ti/Al samples do not present any significant photocatalytic activity. However, calcination at 900 °C leads to a major boost in the photocatalytic activity, while this increased activity falls drastically upon further calcination at 1000 °C. Structural characterization data given in Figs. 2–4 indicate that for calcination temperatures below 900 °C, (P2) 0.5 Ti/Al system is composed of a mostly amorphous $Al_xTi_yO_z$ mixed oxide, which also contains poorly ordered and small anatase and rutile crystallites (Figs. 3b and 4b) rendering a relatively high SSA (i.e. ≥131 m^2/g) (Fig. 2b). Upon calcination of the (P2) 0.5 Ti/Al photocatalyst at 900 °C, formation of an ordered rutile phase, together with a relatively minor contribution from anatase particles (Figs. 3b and 4b) are observed; concomitant to a drastic decrease in SSA to 64 m^2/g (Fig. 2b).

Note that analogous temperature-dependent performance trends are also valid for the (P2) 1.0 Ti/Al family given in Fig. 5, where the onset of the photocatalytic activities observed at a lower temperature of 800 °C with increasing titania loading in the binary oxide system. This minor temperature shift in the onset of photocatalytic activity for the higher titania loading is in line with the shift in the anatase/rutile crystallization temperatures for the (P2) 1.0 Ti/Al samples, discussed above. Furthermore, the decline in the photocatalytic activity of the Ti/Al systems at $T > 900$ °C can be explained with the almost complete loss of the anatase phase (Figs. 3 and 4). It is known that the co-existence of both anatase and rutile phases is critical for obtaining a high photocatalytic NO oxidation and storage activity [34,48,49]. Thus in overall, these observations suggest that although Ti/Al systems calcined at lower temperatures reveal relatively higher SSA, these poorly ordered or amorphous systems do not possess the proper crystallographic/electronic/morphological features required for the generation of the photocatalytic active sites with sufficient quality/quantity.

Comparison of the photocatalytic performance results given in Fig. 5 for the (P1) Ti/Al family with that of (P2) Ti/Al family implies that there is a complex interplay between calcination temperature, crystal structure, composition and SSA which dictate the final photocatalytic activity in a coordinative manner. In order to illustrate this point, one can compare the best performing photocatalyst in the P1 family (e.g. (P1) 0.5 Ti/Al-800) to that of P2 (e.g. (P2) 0.5 Ti/Al-900). It can readily be seen that photocatalytic total NO_x decrease (i.e. blue bars in Fig. 5) for these samples are about 161–176% greater than that of Degussa P25 benchmark photocatalyst while their NO_2 slip to the atmosphere (i.e. red bars in Fig. 5) are significantly lower than that of Degussa P25 (i.e. 75% lower for (P1) 0.5 Ti/Al-800 and 55% lower for (P2) 0.5 Ti/Al-900). In other words, both of these photocatalysts can simultaneously oxidize NO into NO_2 and capture oxidized NO_x species in the solid state in a much more efficient manner than Degussa P25. However, comparison of the structural properties of these two efficient photocatalysts presents stark dissimilarities. Firstly, XRD (Fig. 3a) and Raman (Fig. 4a) data for the (P1) 0.5 Ti/Al-800 sample reveal that this material is predominantly comprised of an anatase phase with a minor contribution from rutile, while corresponding data for the (P2) 0.5 Ti/Al-900 sample (Figs. 3b and 4b) suggest a composition where rutile is the dominant phase with anatase being the minority phase. These two structurally different photocatalysts revealing comparably high photocatalytic activities implies that the photocatalytically active site(s) have a complex nature which may involve an amorphous phase, a particular anatase (or rutile) adsorption site, a particular adsorption site on the anatase/rutile hetero-junction and/or a particular —OH functionality on any of these domains etc. However, it is clear that ordinary XRD and Raman measurements do not reveal unambiguous information regarding neither the nature nor the quantity of such active sites.

It can also be emphasized that these two different but comparably active photocatalysts (i.e. (P1) 0.5 Ti/Al-800 and (P2) 0.5 Ti/Al-900) have quite dissimilar SSA values. While (P1) 0.5 Ti/Al-800 sample have a SSA of 161 m^2/g, (P2) 0.5 Ti/Al-900 sample has a SSA of 64 m^2/g. This observation demonstrates that using absolute SSA values as the sole parameter for comparing the photocatalytic activities of dissimilar materials can be misleading (Supporting Information Fig. S3).

Consequently, results presented in the current work indicate that Ti/Al binary oxide photocatalysts can be synthesized using different synthetic protocols possessing quite different structural features detected in BET, Raman and XRD measurements yet, revealing similar photocatalytic activities. Hence, neither the nature, nor the quantity of the photocatalytic active sites can be readily inferred directly from such conventional and long-range characterization techniques which lack spatial/energetic resolution in the nanometer scale that can locally probe the electronic and structural properties of the particular active site(s).

4. Conclusions

In the current work, TiO_2/Al_2O_3 binary oxide photocatalysts were synthesized via two different sol–gel protocols (P1 and P2) where various TiO_2 to Al_2O_3 mole ratios (0.5 and 1.0) and calcination temperatures (150–1000 °C) were utilized in the synthesis procedures. Structural characterization of the synthesized binary oxide photocatalysts was also performed via BET surface area analysis, X-ray diffraction (XRD) and Raman spectroscopy; and the photocatalytic NO(g) oxidation performances of these binary oxides were measured under UVA irradiation in a comparative fashion to that of Degussa P25 industrial benchmark. TiO_2/Al_2O_3 binary oxide photocatalysts were designed to demonstrate a novel approach which is essentially a fusion of NSR (NO_x Storage Reduction) and PCO (Photocatalytic Oxidation) technologies. In this approach, rather than attempting to perform complete NO_x reduction, NO(g) is oxidized on a photocatalyst surface and stored in the solid state in the form of nitrates/nitrites (or their protonated surface derivatives) on a storage component. Current results suggest that alumina domains can be utilized as active NO_x capturing sites that can significantly eliminate the release of toxic NO_2(g) into the atmosphere by adsorption and solid state storage. Using either P1 or P2 protocols, structurally different Ti/Al binary oxide systems can be synthesized which enable much superior photocatalytic total NO_x removal (i.e. up to 176% higher) than Degussa P25 industrial benchmark. Furthermore, such Ti/Al binary oxides can also decrease the toxic NO_2(g) emission into the atmosphere (which is formed due to the photocatalytic oxidation of NO(g)) by 75% with respect to that of Degussa P25. It is apparent that there is a complex interplay between the calcination temperature, crystal structure, composition and SSA which dictate the ultimate photocatalytic activity in a coordinative manner. It was observed that two structurally different photocatalysts prepared via different preparation protocols may reveal comparably high photocatalytic activities implying that the photocatalytically active sites responsible for the photocatalytic NO(g) oxidation and storage have a non-trivial nature.

Acknowledgements

The authors acknowledge the financial support from the Scientific and Technical Research Council of Turkey (TUBITAK) (Project Code: 109M713). E.O. also acknowledges financial support from Turkish Academy of Sciences through the "TUBA-GEBIP Outstanding Young Scientist Prize" and from Fevzi Akkaya Science Fund (FABED) through Eser Tümen Scientific Achievement Award.

Appendix A. Supplementary data

Supplementary data associated with this article can be found, in the online version, at http://dx.doi.org/10.1016/j.cattod.2014.04.001.

References

[1] T.N. Obee, R.T. Brown, Environ. Sci. Technol. 29 (1995) 1223–1231.
[2] Q.L. Yu, H.J.H. Brouwers, Appl. Catal. B: Environ. 92 (2009) 454–461.
[3] A.R. Ravishankara, Chem. Rev. 103 (2003) 4505–4507.
[4] K. Skalska, J.S. Miller, S. Ledakowicz, Sci. Total Environ. 408 (2010) 3976–3989.
[5] S. Roy, M.S. Hegde, G. Madras, Appl. Energy 86 (2009) 2283–2297.
[6] Toyota Patent, European Patent Application no: 0573 672A1 (1992).
[7] N. Takahashi, H. Shinjoh, T. Iijima, T. Suziki, K. Yamazaki, K. Yokota, H. Suziki, N. Miyoshi, S. Matsumoto, T. Tanizawa, T. Tanaka, S. Tateishi, K. Kasahara, Catal. Today 27 (1996) 63–69.
[8] M.T. Javed, N. Irfan, B.M. Gibbs, J. Environ. Manage. 83 (2007) 251–289.
[9] M.A. Uddin, K. Shimizu, K. Ishibe, E. Sasaoka, J. Mol. Catal. A: Chem. 309 (2009) 178–183.
[10] J.S. Hepburn, E. Thanaslu, D.A. Dobson, W.L. Watkins, SAE Technical Paper (1996) 962051.
[11] S.M. Andonova, G.S. Senturk, E. Kayhan, E. Ozensoy, J. Phys. Chem. C 113 (2009) 11014–11026.
[12] S.M. Andonova, G.S. Senturk, E. Ozensoy, J. Phys. Chem. C 114 (2010) 17003–17016.
[13] T. Tabata, K. Baba, H. Kawashima, Appl. Catal. B: Environ. 7 (1995) 19–32.
[14] J. Lasek, Y.H. Yu, J.C.S. Wu, J. Photochem. Photobiol. C: Photochem. Rev. 14 (2013) 29–52.
[15] S. Devahaddin, C. Fan, K. Li, D.H. Chen, J. Photochem. Photobiol. A: Chem. 156 (2003) 161–170.
[16] M.M. Ballari, M. Hunger, G. Husken, H.J.H. Brouwers, Appl. Catal. B: Environ. 95 (2010) 245–254.
[17] Q.L. Yu, M.M. Ballari, H.J.H. Brouwers, Appl. Catal. B: Environ. 99 (2010) 58–65.
[18] M.R. Hoffman, S.T. Martin, W. Choi, D.W. Bahnemann, Chem. Rev. 95 (1995) 69–96.
[19] N. Meng, M.K.H. Leung, D.Y.C. Leung, K. Sumathy, Renew. Sust. Energ. Rev. 11 (2007) 401–425.
[20] T. Martinez, A. Bertron, E. Ringot, G. Escadeillas, Built Environ. 46 (2011) 1808–1816.
[21] N. Bowering, G.S. Walker, P.G. Harrison, Appl. Catal. B: Environ. 62 (2006) 208–216.
[22] K. Hashimoto, K. Wasada, N. Toukai, H. Kominami, Y. Kera, J. Photochem. Photobiol. A 136 (2000) 103–109.
[23] H. Wang, Z. Wu, W. Zhao, B. Guan, Chemosphere 66 (2007) 185–190.
[24] L. Yang, Y. Wang, L. Zhao, Chin. Opt. Lett. 10 (6) (2012), 063102 (3).
[25] A.D. Paola, G. Cufalo, M. Addamo, M. Bellardita, R. Campostrini, M. Ischia, R. Ceccato, L. Palmisano, Colloids Surf. A: Physicochem. Eng. Aspects 317 (2008) 366–376.
[26] A. Mitsionis, T. Vaimakis, C. Trapalis, N. Todorova, D. Bahnemann, R. Dillert, Appl. Catal. B: Environ. 106 (2011) 398–404.
[27] N. Negishi, K. Takeuchi, T. Ibusuki, J. Sol–Gel Sci. Technol. 13 (1998) 691–694.
[28] C.L. Bianchi, C. Pirola, E. Selli, S. Biella, J. Hazard. Mater. 211–212 (2012) 203–207.
[29] J.S. Dalton, P.A. Janes, N.G. Jones, J.A. Nicholson, K.R. Hallam, G.C. Allen, Environ. Pollut. 120 (2002) 415–422.
[30] A. Fujishima, X. Zhang, D.A. Tryk, Surf. Sci. Rep. 63 (2008) 515582.
[31] W. Wang, Y. Yang, H. Luo, T. Hu, F. Wang, W. Liu, J. Alloys Compd. 509 (2011) 3430–3434.
[32] B.N. Shelimov, N.N. Tolkachev, O.P. Tkachenko, G.N. Baeva, K.V. Klementiev, A.Yu. Stakheev, V.B. Kazansky, J. Photochem. Photobiol. A 195 (2008) 81–88.
[33] A.M. Soylu, M. Polat, D.A. Erdogan, C. Yildirim, O. Birer, E. Ozensoy, Applied Surface Science, 2014, In Press, Corrected Proof, http://dx.doi.org/10.1016/j.apsusc.2014.02.065.
[34] A. Folli, S.B. Campbell, J.A. Anderson, D.E. Macphee, J. Photochem. Photobiol. A 220 (2011) 85–93.
[35] G.S. Senturk, E.I. Vovk, V.I. Zaikovskii, Z. Say, A.M. Soylu, V.I. Buktiyarov, E. Ozensoy, Catal. Today 184 (2012) 54–71.
[36] M. Nargiello, T. Herz, Physical–chemical characteristics of P-25making it extremely suited as the catalyst in photodegradation oforganic-compounds, in: B.V. Amsterdam (Ed.), Photocatalytic Purification and Treatment of Water and Air, vol. 3, Elsevier Science Publication, 1993, pp. 801–807.
[37] D.A. Erdogan, M. Polat, R. Garifullin, M.O. Guler, E. Ozensoy, Applied Surface Science, 2014, In Press, Accepted Manuscript, http://dx.doi.org/10.1016/j.apsusc.2014.04.082.
[38] I.E. Wachs, S.P. Phivilay, C.A. Roberts, ACS Catal. 3 (2013) 2606–2611.
[39] M. Anpo, T. Kawamura, S. Kodama, J. Phys. Chem. 92 (1988) 438–440.
[40] M. Anpo, M. Takeuchi, J. Catal. 216 (2003) 505–516.
[41] C. Anderson, A.J. Bard, J. Phys. Chem. B 101 (1997) 2611–2616.
[42] V. Loddo, G. Marci, L. Palmisano, A. Sclafani, Mater. Chem. Phys. 53 (1998) 217–224.
[43] H. Nishiguchi, J-L. Zhang, M. Anpo, H. Masuhara, J. Phys. Chem. B 105 (2001) 3218–3222.
[44] M.I. Franch, J. Peral, X. Domenech, R.F. Howe, J.A. Ayllon, Appl. Catal. B 55 (2005) 105–113.
[45] M. Kitano, M. Matsuoka, M. Ueshima, M. Anpo, Appl. Catal. A 325 (2007) 1–14.
[46] B.N. Shelimov, N.N. Tolkachev, O.P. Tkachenko, G.N. Baeva, K.V. Klementiev, A.Y. Stakheev, V.B. Kazansky, J. Photochem. Photobiol. A: Chem. 195 (2008) 81–88.
[47] O. Carp, C.L. Huisman, A. Reller, Prog. Solid State Chem. 32 (2004) 33–177.
[48] D.O. Scanlon, C.W. Dunnill, J. Buckeridge, S.A. Shevlin, A.J. Logsdail, S.M. Woodley, C.R.A. Catlow, M.J. Powell, R.G. Palgrave, I.P. Parkin, G.W. Watson, T.W. Keal, P. Sherwood, A. Walsh, A.A. Sokol, Nat. Mater. 12 (2013) 798–801.
[49] T. Luttrell, S. Halpegamage, J. Tao, A. Kramer, E. Sutter, M. Batzill, Sci. Rep. 4 (2014) 1–8.